

Hypervelocity Impact of Additively Manufactured A356/316L Interpenetrating Phase Composites

M.R. French¹, W.A. Yarberr III¹, A.E. Pawlowski^{2,3}, A. Shyam⁴, D.A. Splitter², A.M. Elliott⁵,
J.K. Carver⁴, Z.C. Cordero¹

1. Materials Science and NanoEngineering, Rice University, Houston, TX 77005
2. Fuels, Engines and Emissions Research Center, ORNL, Knoxville, TN 37932
3. Bredesen Center, University of Tennessee-Knoxville, Knoxville, TN 37996
4. Materials Science and Technology Division, ORNL, Oak Ridge, TN 37831
5. Energy and Transportation Science Division, ORNL, Oak Ridge, TN 37831

Corresponding Author: Zachary Cordero; zc29@rice.edu; 713-348-2495

Abstract: We have examined the hypervelocity impact response of targets made from monolithic A356 and 316L stainless steel, as well as an additively manufactured A356/316L interpenetrating phase composite. 1.9 mm diameter spherical projectiles made from 2017 aluminum were fired at velocities of 5.9-6.1 km/s, allowing for the observation of multiple types of macro- and microstructural damage within each target. The macroscopic cratering damage to the A356/316L composite resembles that of the A356, but observations of both the cross section and the microstructural damage suggest that the A356/316L composite may be more resistant to spalling than A356 shielding with the same areal density.

1. Introduction

In a recent study, we described a two-step approach for synthesizing net-shaped metallic composites [1]. In the first step of this approach, selective laser melting is used to fabricate a lattice preform that serves as the reinforcement. In the second step, this lattice preform is liquid metal infiltrated with a second material that has a melting point lower than that of the lattice. The resulting part is an interpenetrating phase composite (IPC) in which both constituents form continuous networks. This print-and-infiltrate approach offers two key advantages over other techniques for synthesizing metallic composites. First, because this approach excludes liquid-phase mixing of the constituents, it largely avoids the problems with intermetallic formation that limit other fusion-based techniques for printing metallic composites [2]. Second, it can pattern the constituents with a resolution on the order of 100 μm , or at least an order of magnitude finer than that of fusion-based techniques that require changing the feedstock composition during printing [3].

In our preliminary studies, we have used this two-step processing route to fabricate proof-of-concept composites of 316L stainless steel and a heat-treatable aluminum casting alloy, A356. In this case the 316L is the reinforcement and the A356 is the infiltrant. These first-generation A356/316L composites can have low densities ($<4.10 \text{ g/cm}^3$), respectable yield strengths (140-250 MPa), higher thermal conductivities compared to 316L (44 W/m K), and exceptional damage tolerance under tensile loading. For example, tension tests on composites containing 38 vol% 316L

showed a strain-to-failure of 32%, representing an order of magnitude improvement over the strain-to-failure of monolithic A356 [1].

This preliminary work demonstrated that these additively manufactured composites exhibit a suite of properties that makes them especially attractive candidates for lightweight armor used in multiple-hit aerospace applications. Motivated by these findings, the objective of this study was to evaluate the hypervelocity impact response of these additively manufactured A356/316L IPCs and to compare their performance with those of the constituent materials. Hypervelocity impacts are of special importance in aerospace shielding applications, where shielding materials are routinely impacted by dust and debris orbiting the Earth at speeds of over 5 km/s [4].

2. Experimental Methods

2.1. Materials Processing

We evaluated the hypervelocity impact response of an additively manufactured 38 vol% 316L composite prepared using the method described in [1]. First, we printed the 316L lattice preforms using a Renishaw AM250 selective laser melting system, using a feedstock of gas-atomized 316L powder (Fe-18Cr-12-Ni-2Mo, wt%). The lattice had body centered cubic symmetry, with the unit cell geometry shown schematically in **Figure 1**. The unit cell edge-length was 2.5 mm, and the 316L strut diameter was 0.8 mm. Next, we used centrifugal casting to infiltrate the lattice preforms with A356. Prior to impact testing, the strike face and rear surface of the composite targets were face-milled and polished to mirror finish. For comparison purposes, we also performed impact tests on cold-rolled 316L and as-cast A356. The final dimensions of the 316L, A356, and composite targets were 41x40x12.5 mm³, 40x39x12 mm³, and 38x36x10.9 mm³, respectively. **Table 1** summarizes the densities of the cold-rolled 316L, as-cast A356, and A356/316L IPC. **Table 1** also includes the Vickers microhardness values for the cold-rolled 316L, as-cast A356, and the constituents of the IPC. The microhardness tests were performed under a load of 300 gf.

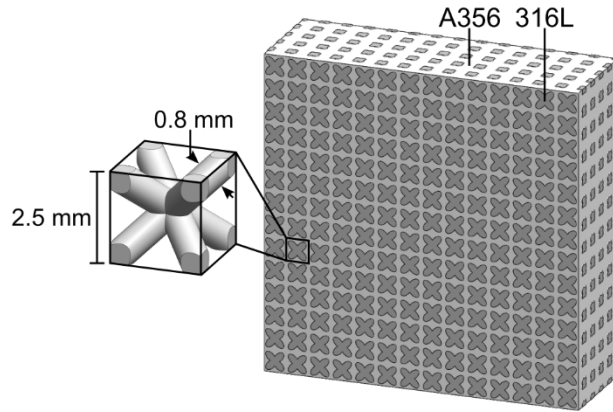


Figure 1: Interpenetrating phase composite and inset showing the unit cell geometry.

Table 1: Density and Vickers hardness of target materials.

	Density (g/cm ³)	Hardness (GPa)	Areal Density (g/cm ²)
Cold-Rolled 316L	7.97	1.74	9.96
316L Reinforcement	–	2.34	–
Cast A356	2.70	0.76	3.24
A356 Infiltrant	–	0.98	–
38 vol% 316L Composite	4.71	–	5.14

2.2. Hypervelocity Impact Setup

We used hypervelocity impact tests to compare the impact performance of the A356/316L composite to the performance of its constituents, A356 and 316L. We conducted the hypervelocity impact tests using an 0.17 caliber two-stage light-gas gun, which has the capability to propel small projectiles at speeds of up to 7 km/s. The two-stage light-gas gun achieves these velocities by first detonating a charge of smokeless gunpowder inside a pump tube, expanding against a piston. This then forces the piston into a volume of hydrogen gas, bringing that gas under immense pressures, on the order of 10^{-1} GPa [5]. The compressed hydrogen accelerates the projectile and its nylon sabot down the length of the barrel. The sabot discards from the projectile as it leaves the barrel, and the projectile interrupts multiple laser/photodiode intervalometers, allowing the velocity of the projectile to be recorded.

Each test used a 1.9 mm diameter sphere of 2017 aluminum as a projectile, which will produce impacts representative of those caused by micrometeoroids and orbital debris [4]. The measured velocities and calculated projectile kinetic energies are summarized in **Table 2**. The projectiles struck the targets at normal incidence.

Table 2: Velocity and kinetic energy of aluminum projectile.

	Velocity (km/s)	Kinetic Energy (J)
316L	6.0	180
A356	5.9	176
38 vol% 316L Composite	6.1	186

2.3. Impact Characterization:

After each impact test, we removed the gunpowder residue from the samples in an ultrasonic cleaning bath containing isopropanol. We performed optical profilometry on the craters using a Keyence VR-3000 Wide-Area 3D measurement system. Following the profilometry, we performed postmortem analysis on the impact targets using a FEI Quanta 400 SEM and a JEOL JSM-6560 SEM. Finally, we cross-sectioned, mounted, and polished the targets, and then examined the crater using optical microscopy. The 316L cross-sections were etched in 5% Nital to reveal grain structure.

3. Results and Discussion

After each material underwent impact testing, the three targets were characterized using standard metallographic procedures. Crater dimensions provide a simple metric for comparing the amount of damage each material sustains after it undergoes hypervelocity impact. Typical hypervelocity impacts display hemispherical, symmetric craters with a depth roughly half of their width [4]. The dimensions of the craters in the different target materials are listed in **Table 3**. The morphology of the craters and the microstructure in the impact zone are described in more detail below. Evidence of localized melting is present in every crater, as the contact temperatures during impact can easily exceed 1000 K [6].

Table 3: Macroscopic target damage data

	Crater Volume (mm ³)	Crater Depth (mm)	Crater Width (mm)
316L	25	2.0	5.1
A356	117	4.5	7.2
38 vol% 316L Composite	96	4.4	6.8

3.1. Damage Observed in 316L Stainless Steel

Figure 2 is a low magnification SEM image of the 316L target's crater. The hemispherical, symmetric crater shows a petalled lip typical of hypervelocity impact into ductile materials [7]. There was no fragmented material surrounding the crater, and no cracks were present outside of the crater. The crater depth was 1.05x larger than the projectile diameter, and the crater width was 2.7x the projectile diameter. Overall, there was only localized macroscopic damage on the 316L impact surface. Profilometry showed a 16 μm tall bulge protruding from the rear surface.

Higher magnification SEM images revealed some of the damage mechanisms in the 316L. Slip traces with spacings on the order of 0.1-5 μm were visible in a zone 0.5 mm around the petalled lip of the crater. Inside the crater, a uniform layer of aluminum with a 1 μm grain size was deposited as a result of projectile vaporization. The inside of the crater displayed many small steps, similar to those identified by Shockey *et al.*, who suggested that these steps result from shear bands that terminate on the inner surface of the crater [8].

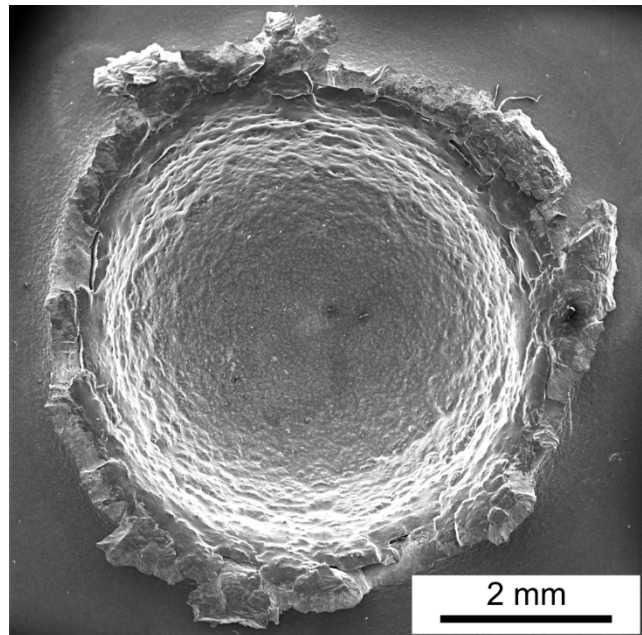


Figure 2: Low magnification SEM image of damage to the front surface of 316L target

A cross-section micrograph of the polished and etched 316L is shown in **Figure 3**. There was no evidence of internal cracking. A small zone of plastic deformation was revealed, extending roughly 0.5 mm beyond the crater's face, identical to the width of the zone displaying slip traces outside the crater. No spalling or cracking was observed on the back face of this target.

3.2. Damage Observed in As-cast A356

Figure 4 is a low magnification SEM image of the crater in the A356 target. Inspection of the A356 shows that it sustained significantly more damage than the 316L. The hemispherical crater is 3.8x wider and 2.4x deeper than the projectile. Additionally, the crater volume of the A356 is 4.7x that of the 316L target's crater. There are cracks visible on the surface, and the petalled lip that surrounded the crater in the 316L is absent in the A356. This lip is not present in the A356 target because the material ejected from the crater fractured as a result of the extensive plastic strains generated on impact.

Visual inspection of the rear surface of the A356 target also showed extensive damage, due to incipient spall, creating a cracked dimple that extends a distance of 0.7 mm from the rear surface. A compressive shockwave is created as the projectile impinges upon the target, which travels towards the rear face of the target. When this compressive wave reaches the rear surface, it reflects as a tensile wave that travels back towards the strike face. Spall occurs when the magnitude of the tensile stress in this reflected shock wave exceeds the ultimate dynamic tensile strength of the material [9]. For impacts between spherical projectiles and flat targets, this spalling criterion is met along a spherical section projected outwards from the crater, with a distance from the rear surface of 10-50% of the thickness of the plate [4]. Spall is capable of causing extensive damage, even if the target is not perforated by the projectile, and is a major concern in both spaceflight and military armor applications. In this test, material did not detach from the back face, but the large, bulged region, approximately 9.4 mm in diameter, is filled with extensive cracks. This suggests that the spall carried almost enough momentum to cause complete detachment from the rear surface of the target.

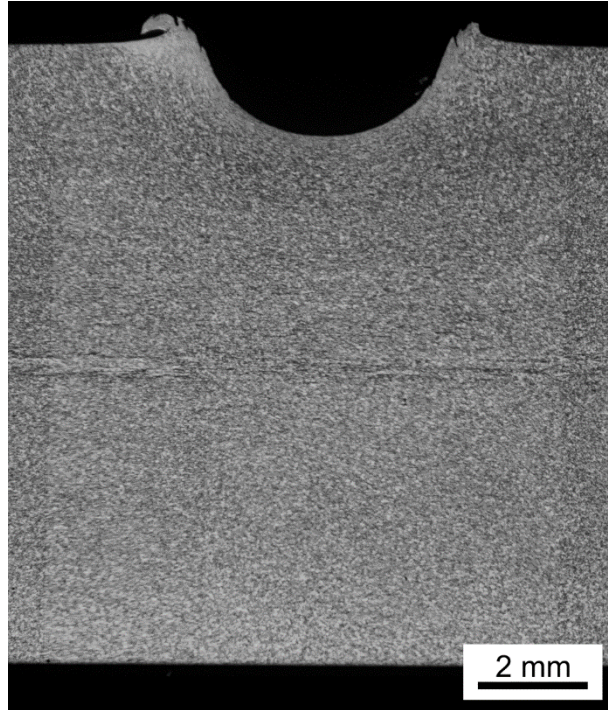


Figure 3: Optical image of the cross-sectioned, polished and etched 316L target.

Postmortem analysis conducted on the A356 target showed damage mechanisms similar to those

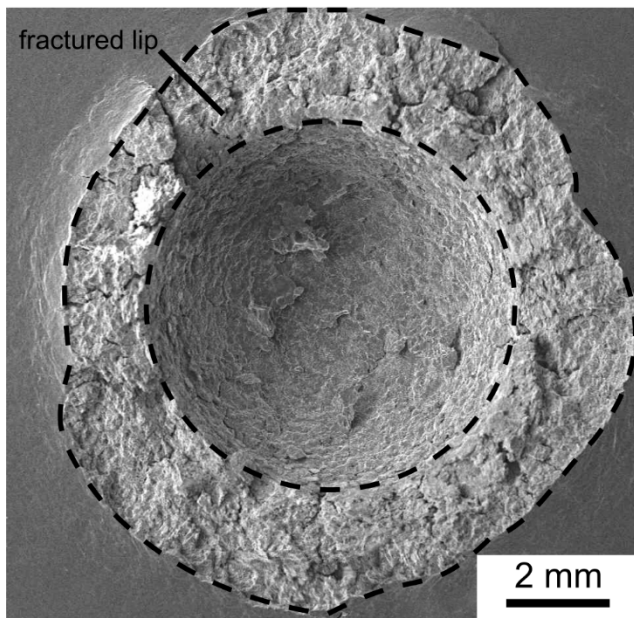


Figure 4: Low magnification SEM image of damage to the front surface observed on A356 target.

found in quasi-static testing of A356, with cracks propagating along the brittle silicon eutectic particles in the interdendritic regions [10]. In the annular region surrounding the crater, the material showed cleavage facets, as cracks propagated between primary aluminum grains, then through interdendritic regions rich in brittle silicon particles. Small cracks were clearly visible on the strike face of the target, and extended at least 2 mm beyond the edge of the fractured lip. Within the individual aluminum grains in this region, slip traces with $\sim 2 \mu\text{m}$ spacing were commonly observed. The interior of the A356 crater was slightly less uniform than the interior of the 316L crater, with deposits of projectile material forming small masses at the bottom of the crater. Towards the top of the crater there was

evidence of brittle fracture identical to that of the fractured region at the top of the crater. On the back face of the specimen, the cracks propagated through the interdendritic regions. The damage modes seen in our specimens are broadly consistent with those reported by Brewer et al. [11] and Wang et al. [12] in their respective studies on impact into aluminum and aluminum alloys.

Analysis of the A356 target's cross section, shown in **Figure 5**, revealed extensive microcracking distributed through the thickness of the target. The incipient spall plane was 1.5 mm from the back face and was approximately 1 cm in diameter. Many cracks were present, the largest of which were ~2 mm long. The largest cracks were oriented parallel to the strike face but there were also many small cracks that were perpendicular to the strike face and that traveled through interdendritic regions between the primary aluminum grains. A region of intense plastic deformation, where the dendrites were extremely compressed, extended 1 mm away from the crater wall. These observations show that the A356 was severely damaged by the impact, and that it would perform poorly in multiple-hit applications.

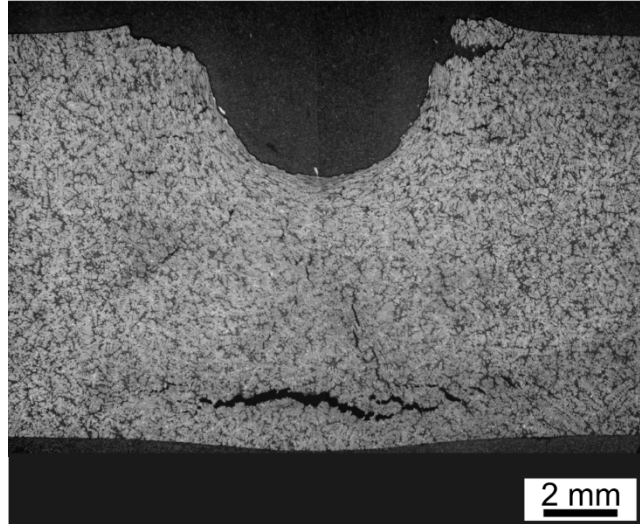


Figure 5: Optical image of the cross-sectioned and polished A356 target.

3.3. Damage Observed in 38 vol% 316L Composite

The surface of the A356/316L composite showed a variety of damage modes, reflecting the disparate impact behaviors of the two component materials. The SEM image of the crater in **Figure 6** shows that the crater was square in shape rather than circular, reflecting the symmetry of the lattice. There was neither a large raised lip, as in the 316L target, nor a significant fractured region, as in the A356 target. The square crater was 3.6x wider and 2.3x deeper than the projectile, or approximately 3 unit cells wide and 1 unit cell deep. The A356 at the edge of the crater eroded 1 mm further than the steel, as the steel shielded the remainder of the A356 from damage. Profilometry on the rear surface of the target revealed that the aluminum was slightly extruded through the steel, and that the bulge on the composite was only slightly higher than the bulge on the rear surface of the 316L target, which was also 1.6 mm thicker than the composite.

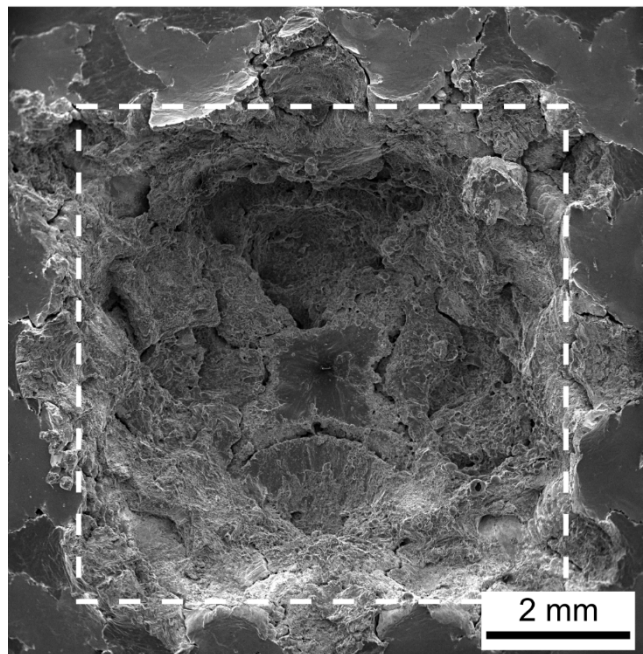


Figure 6: Low magnification SEM image of damage to front surface of the A356/316L target.

Close inspection of the composite revealed that it shared some traits in common with the 316L and A356 targets, but that the crater in the composite was not nearly as uniform as the craters in the two monolithic targets. The A356 in the composite appeared to have fractured at the edge of the crater, displaying crevices approximately 0.5 mm deep between the 316L struts. This region showed the same fracture mechanisms as the A356: a combination of brittle cleavage and intergranular fracture between the primary aluminum grains. Likewise, the steel showed evidence of plastic deformation in the struts surrounding the crater, with similarly spaced slip traces present in both the printed and as-received 316L. No surface cracking was present in the aluminum outside the eroded and plastically deformed region, and the only cracks present in the steel were localized to small cracks between pores in the single unit cell adjacent to the crater edge. The tips of the upturned struts in the composite specimen resemble the petalled lips of the monolithic 316L crater, with fine ductile dimples found on the surface where failure occurred.

The cross-section micrograph of the A356/316L composite shown in **Figure 7** reveals some of the unique damage modes in these IPC shielding elements. One interesting feature is the morphology of the 316L struts. The struts deformed upon impact, spreading apart from the center of the unit cell, and forming a protective coating over the A356. This deformation and protection occurred as a direct result of the crater's rapid expansion. As material was driven out of the crater, the aluminum ruptured and was ejected, leaving behind the angled steel struts, which were oriented so that when they deformed with the expanding crater, they bent outwards from the center, increasing

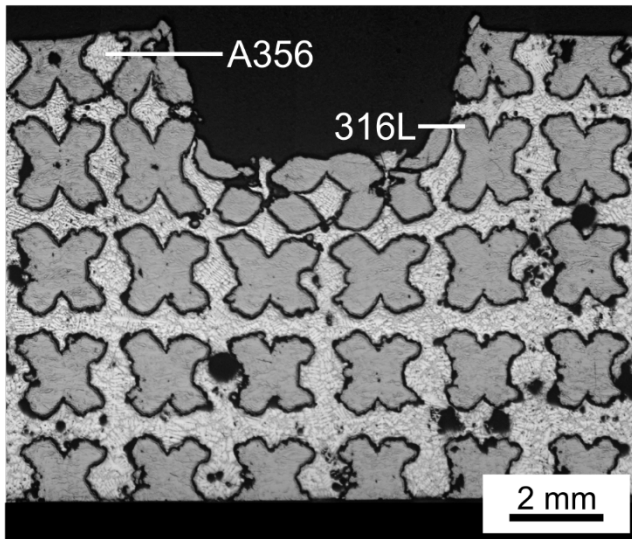


Figure 7: Optical image of the cross-sectioned and polished A356/316L composite target.

the local areal density and resistance to further deformation, halting the expansion of the crater. **Figure 7** shows that plastic deformation was limited to the unit cell adjacent to the impact, and that there was no cracking present in either the 316L or the A356. In addition, there was no evidence of spall in the composite material under this set of test parameters. We hypothesize that this may be because the compressive shockwave generated on impact is attenuated as it travels through the composite, as it closes pores and other residual defects. Because there is no damage evident in the region outside of the immediate vicinity of the crater, these results demonstrate the potential for this material to withstand multiple hits.

4. Summary

We have developed an additively manufactured A356/316L IPC that may offer improved shielding performance for air- and spacecraft when compared to either A356 or 316L monolithic armor, by remaining lightweight while localizing damage to a small area. This composite has demonstrated increased spall-resistance when compared to monolithic A356, and microstructural damage does not appear to occur outside of the immediate vicinity of the crater. In many different metrics of

shielding performance, this material behaves well, due to its unique traits resulting in the composite efficiently dissipating the kinetic energy of the projectile.

Acknowledgements

The authors wish to thank R. J. McCandless of Jacobs Technology for valuable assistance in operating the light-gas gun, and T. Seabury of ExxonMobil for helping with the metallographic investigations. This project was supported by the U.S. Department of Energy, Office of Energy Efficiency and Renewable Energy, Vehicle Technologies Office, as part of the Propulsion Materials Program.

This manuscript has been authored by UT-Battelle, LLC under Contract No. DE-AC05-00OR22725 with the U.S. Department of Energy. The United States Government retains and the publisher, by accepting the article for publication, acknowledges that the United States Government retains a non-exclusive, paid-up, irrevocable, world-wide license to publish or reproduce the published form of this manuscript, or allow others to do so, for United States Government purposes. The Department of Energy will provide public access to these results of federally sponsored research in accordance with the DOE Public Access Plan (<http://energy.gov/downloads/doe-public-access-plan>).

References

- [1] A.E. Pawlowski, Z.C. Cordero, M.R. French, T.R. Muth, J. Keith Carver, R.B. Dinwiddie, A.M. Elliott, A. Shyam, D.A. Splitter, Damage-tolerant metallic composites via melt infiltration of additively manufactured preforms, *Mater. Des.* 127 (2017) 346–351. doi:10.1016/j.matdes.2017.04.072.
- [2] L.D. Bobbio, R.A. Otis, J.P. Borgonia, R.P. Dillon, A.A. Shapiro, Z.-K. Liu, A.M. Beese, Additive manufacturing of a functionally graded material from Ti-6Al-4V to Invar: Experimental characterization and thermodynamic calculations, *Acta Mater.* 127 (2017) 133–142. doi:10.1016/j.actamat.2016.12.070.
- [3] B.E. Carroll, R.A. Otis, J.P. Borgonia, J. Suh, R.P. Dillon, A.A. Shapiro, D.C. Hofmann, Z.-K. Liu, A.M. Beese, Functionally graded material of 304L stainless steel and inconel 625 fabricated by directed energy deposition: Characterization and thermodynamic modeling, *Acta Mater.* 108 (2016) 46–54. doi:10.1016/j.actamat.2016.02.019.
- [4] D.R. Christman, J.W. Gehring, C.J. Maiden, A.B. Wenzel, Study of the phenomena of hypervelocity impact, DTIC, 1963.
- [5] D.E. Munson, R.P. May, Interior ballistics of a two-stage light gas gun using velocity interferometry, *AIAA J.* 14 (1976) 235–242. doi:10.2514/3.7075.
- [6] R.L. Bjork, A.E. Olshaker, The role of melting and vaporization in hypervelocity impact, DTIC, 1965.
- [7] B.G. Cour-Palais, Hypervelocity impact in metals, glass and composites, *Int. J. Impact Eng.* 5 (1987) 221–237. doi:10.1016/0734-743X(87)90040-6.
- [8] D.A. Shockey, D.R. Curran, P.S. De Carli, Damage in steel plates from hypervelocity impact. I. Physical changes and effects of projectile material, *J. Appl. Phys.* 46 (1975) 3766–3775. doi:10.1063/1.322162.
- [9] W. Herrmann, J.S. Wilbeck, Review of hypervelocity penetration theories, *Int. J. Impact Eng.* 5 (1987) 307–322. doi:10.1016/0734-743X(87)90048-0.
- [10] Q.G. Wang, Microstructural effects on the tensile and fracture behavior of aluminum casting alloys A356/357, *Metall. Mater. Trans. A.* 34 (2003) 2887–2899. doi:10.1007/s11661-003-0189-7.
- [11] J.L. Brewer, D.A. Dalton, E.D. Jackson, A.C. Bernstein, W. Grigsby, E.M. Taleff, T. Ditmire, Influence of microstructure on the spall failure of aluminum materials, *Metall. Mater. Trans. A.* 38 (2007) 2666–2673. doi:10.1007/s11661-007-9205-7.
- [12] Y. Wang, M. Qi, H. He, L. Wang, Spall failure of aluminum materials with different microstructures, *Mech. Mater.* 69 (2014) 270–279. doi:10.1016/j.mechmat.2013.11.005.